



Interfacial-engineered cobalt@carbon hybrids for synergistically boosted evolution of sulfate radicals toward green oxidation



Xiaoguang Duan^a, Jian Kang^b, Wenjie Tian^a, Huayang Zhang^a, Shih-Hsin Ho^c, Yi-An Zhu^d, Zhimin Ao^e, Hongqi Sun^f, Shaobin Wang^{a,b,*}

^a School of Chemical Engineering, The University of Adelaide, Adelaide, SA 5005, Australia

^b Department of Chemical Engineering, Curtin University, Perth, WA 6845, Australia

^c State Key Laboratory of Urban Water Resource and Environment, School of Environment, Harbin Institute of Technology, Harbin, PR China

^d State Key Laboratory of Chemical Engineering, East China University of Science and Technology (ECUST), Shanghai 200237, PR China

^e School of Environmental Science and Engineering, Institute of Environmental Health and Pollution Control, Guangdong University of Technology, Guangzhou 510006, PR China

^f School of Engineering, Edith Cowan University, Joondalup, WA 6027, Australia

ARTICLE INFO

Keywords:

Nanocomposites
Peroxymonosulfate
Sulfate radical
Nitrogen doping
Metal encapsulation

ABSTRACT

Efficient water remediation relies on robust and capable catalysts to drive the cutting-edge purification technologies. In this work, Prussian blue analogues (PBA) are engaged as the starting materials to fabricate various transition metal (TM)@carbon composites for water decontamination. The encapsulated metallic cobalt is unveiled to be more favorable to deliver electrons to the adjacent carbons than CoP and Co₃O₄, due to the low work function, high conductivity and formation of multiple Co-C bonds for electron tunnelling. Such a hybrid structure significantly tailors the electron density of the carbon lattice, which is the decisive factor influencing activating peroxymonosulfate (PMS) to generate highly reactive sulfate radicals for degradation of contaminants, meanwhile achieving outstanding long-term stability. Deliberate material design and theoretical computations unveil the structure-activity regimes of the composite materials in promoted carbocatalysis. This proof-of-concept study dedicates to elucidating the principles in developing fine-tuned and high-performance TM@carbon hybrids for advanced catalytic oxidation.

1. Introduction

Advanced oxidation processes (AOPs) are powerful techniques to exploit highly reactive oxygen species (ROS) such as sulfate (SO₄²⁻) and hydroxyl (·OH) radicals for chemical oxidation of micro-contaminants into harmless mineralized products [1–3]. Transition metals (TM) and their oxides have been extensively engaged in AOPs to catalyze diverse peroxides to produce ROS. The polyvalent metals can easily coordinate a redox process and their tunable electronic states can be governed by the local metal coordination environments (e.g. structure, composition, facet and morphology) [4–6]. Furthermore, recent studies demonstrate that nanostructured carbon materials (such as graphene, carbon nanotubes, and graphitized nanodiamonds) can activate persulfates such as peroxymonosulfate (PMS) and peroxydisulfate (PDS) to generate ROS for organic oxidation [7–10]. The carbocatalysis stems from the functional groups, defects/edges and heteroatom dopants, which break the chemical inertness of sp² carbon network and

serve as the active sites in catalytic reactions [11,12]. Surface and/or structural engineered nanocarbons in a robust framework demonstrate a superior activity to the metal catalysts, and more importantly, exhibit great stability and would not induce secondary contamination by toxic metal-leaching in strong acid/basic conditions.

Moreover, building heterostructures by encapsulating transition metal nanoparticles (TM-NPs) inside graphitic carbon layers can further boost the carbocatalysis due to the optimized work function, electron configuration, and density of state at Fermi level of the exterior carbon lattice via an electron tunneling effect at the interface of the composites [13,14]. Such metal@carbon nanohybrids are particularly appealing in materials community, as the composites bear all the properties of each compound and can exhibit fascinating new features due to the coupling effect by metal–carbon interactions. Embedding TM-NPs (Co, Fe, Ni) into carbon nanotubes (CNT) renders the CNT as a magnetic nanomaterial, meanwhile the reactivity can be considerably promoted in PMS activation for aqueous oxidation attributing to the synergy of

* Corresponding author at: School of Chemical Engineering, The University of Adelaide, Adelaide, SA 5005, Australia.

E-mail address: shaobin.wang@adelaide.edu.au (S. Wang).

carbocatalysis and hybrid effect [15–19]. Upon the formation of TM@carbon composites, the underlying TM-NPs would donate electrons to the carbon lattice via the intimately interacted metal–carbon interfaces, which can increase the electron density, reduce the local work function, and elevate the Fermi level of the external graphene for enhanced catalysis [14,20]. The number of carbon layers may influence the penetration of metal d electrons, subsequently defining the communications between the TM core and outermost carbon shells [21,22]. Additionally, simultaneous heteroatom doping (B, N, P, and S) into the carbon lattice can further enhance the interactions of the composites and tailor the electron and spin densities of surrounding carbon atoms in chemical reactions [23–25]. Therefore, the TM@carbon-driven AOPs still depend on carbocatalysis in nature, and the catalytic activity of the carbon lattice can be collaboratively manipulated by the local chemistry of carbon and the encapsulated metal species.

Nevertheless, various TM@carbon composites have been fabricated and extensively applied in heterogeneous reactions, there is still lack of an in-depth investigation to unveil the protocols that the TMs' species and properties govern the interfacial electron migration processes and consequently regulate the reactivity of sp^2 carbons to realize satisfactory catalytic behaviors. To this end, a series of TM@carbon composites are developed in this work with controlled metal species (in metallic, oxide and phosphide states) from Fe/Co Prussian blue analogues (PBA). PBA typically presents a molecular formula of $A^{II}[B^{III}(CN)_6]$ (denoted as PBA-AB) with an A-C-N-B configuration in a cubic structure, where A is in a low-spin and low-valence state whereas B possesses a high-spin density with rich electron vacancies [26]. PBA can be synthesized under mild conditions and the categories of the two metal sites are flexible. In this work, the hybrid materials derived from PBA are evaluated for activating PMS to decompose phenolic contaminants in water. The intrinsic reactive species will be identified by selectively radical screening strategy. Density functional theory (DFT) calculations are performed to elucidate the synergistic effects of TM@carbon composites toward enhanced PMS activation. The outcomes are expected to advance the knowledge of rationally regulating the carbocatalysis of hybrid materials by interfacial engineering.

2. Experimental

2.1. Chemicals

The chemicals were obtained from Sigma-Aldrich, Australia, including cobalt (II) chloride ($CoCl_2$), ferrous (II) chloride ($FeCl_2$), potassium hexacyanocobaltate (III, $K_3Co(CN)_6$), potassium hexacyanoferrate (III, $K_3Fe(CN)_6$), phenol, potassium peroxymonosulfate (Oxone[®], $KHSO_5 \cdot 0.5KHSO_4 \cdot 0.5K_2SO_4$), tert-butanol, methanol, 5,5-dimethyl-1-pyrroline N-oxide (DMPO), sodium phosphate monobasic (NaH_2PO_4), and hydrochloric acid (37 wt.%, ACS reagent).

2.2. Synthesis of Fe/Co Prussian blue analogues (PBA) and derived carbocatalysts

In a typical synthesis of PBA-CoCo, 250 mL of $K_3Co(CN)_6$ (30 mM) was dropwise added into 250 mL of $CoCl_2$ (30 mM) solution maintained

at 35 °C via a peristaltic pump at a flowing rate of 2 mL/min. Then a pink suspension was derived. The solid product was separated by a centrifuge at 7500 rpm and dried in an oven at 60 °C. PBA-CoFe was prepared in a similar procedure by replacing $K_3Co(CN)_6$ with $K_3Fe(CN)_6$. PBA-FeFe was prepared using $K_3Fe(CN)_6$ and $FeCl_2$. To derive Co@carbon composites, PBA-CoCo was placed in a tubular quartz reactor, heated under nitrogen at a ramping rate of 2 °C/min, and held at 500 °C for 2 h and then cooled down naturally to room temperature. CoP@carbon was synthesized by placing 100 mg NaH_2PO_4 and 100 mg Co@carbon separately in a quartz boat and annealed under nitrogen atmosphere at a ramping rate of 2 °C/min, and held at 300 °C for 3 h. Co_3O_4 @carbon was synthesized by annealing Co@carbon in a muffle furnace at a ramping rate of 5 °C/min and held at 300 °C in static air for 2 h. Likewise, CoFe@carbon, CoFeP_x@carbon, CoFeOx@carbon, Fe@carbon, FeP@carbon, FeO_x@carbon were prepared using the similar approach from different PBA precursors.

2.3. Characterizations of carbon materials

The structure of materials was revealed by high-resolution transmission electron microscopy (HRTEM) images acquired on a Titan G2 TEM. X-ray photoelectron spectroscopy (XPS) was employed to detect the surface chemical compositions of the carbocatalysts under ultrahigh vacuum conditions in a Kratos AXIS Ultra DLD system. The surface area and porous structure were analyzed at -196 °C on a TriStar instrument and calculated by the Brunauer-Emmett-Teller and Barret-Joyner-Halenda equations. The crystallinity of the carbon materials and hybrids was analyzed by X-ray diffraction (XRD) with a Cu K α X-ray gun at $\lambda = 1.542 \text{ \AA}$.

2.4. Catalytic performance evaluation

The experiment was conducted in a batch reactor with the simultaneous addition of carbocatalysts, organic pollutant, and PMS. The system was maintained at 25 °C in a water bath whilst stirring as a uniform suspension. For the analysis of the concentration of the organics, the solution mixture was filtered through a 0.45 μm PTFE membrane to separate the catalyst and methanol was immediately injected into the system to scavenge the remaining radicals. Phenol was detected on a high-performance liquid chromatography (HPLC, Thermal Fisher) by an OA column under the UV detector at 270 nm.

3. Results and discussion

3.1. Catalyst characterization and performance

As illustrated in Fig. 1, PBA-CoCo is firstly synthesized under mild conditions (synthesis procedure is detailed in the Supplementary Data), and is then treated under an inert atmosphere to yield Co@carbon hybrids. The encapsulated metallic cobalt can be further transferred to cobalt phosphide (CoP@carbon) and oxide (Co_3O_4 @carbon) by post-treatment. Apart from cobalt and oxides which are the benchmark catalysts in PMS activation, CoP has been extensively applied in redox reactions, rendering it great potential as a persulfate activator.

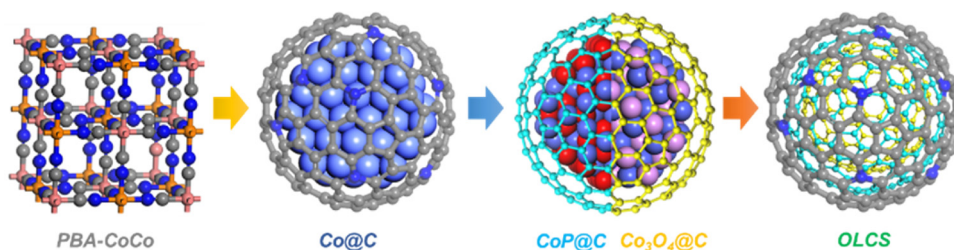


Fig. 1. Illustration of transformation of PBA-CoCo into TM@carbon hybrids and onion-like carbon spheres (OLCS).

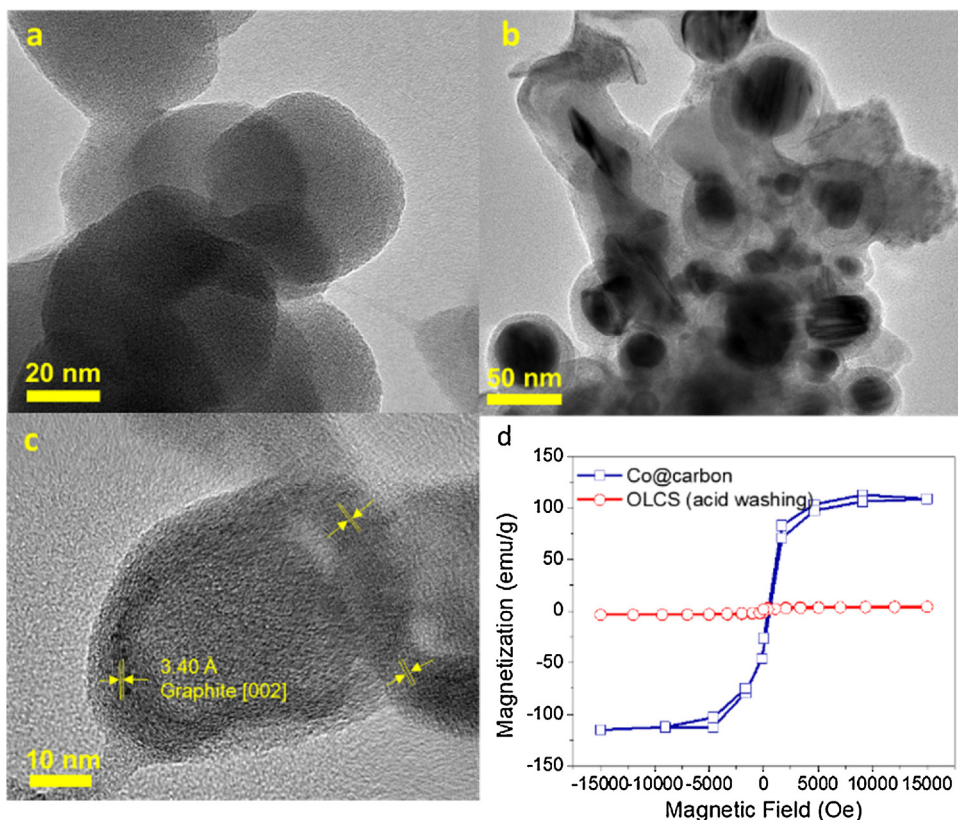


Fig. 2. HRTEM images of (a) PBA-CoCo, (b) Co@carbon, (c) OLCS (after acid washing), and magnetization behavior (d).

Fig. 2a-c display the high-resolution transmission electron microscopy HRTEM images of PBA-CoCo, Co@carbon, onion-like carbon sphere (OLCS, after removal of the metallic core by acid pickling). PBA-CoCo exhibits a spherical morphology with low crystallinity (Figs. 2a and S1). In contrast, a hybrid architecture is clearly observed in Fig. S2 for Co@carbon with a metallic Co [111] terminated core and multiple [002] orientated graphitic shells. The metal core can be completely removed by thorough acid pickling to form a hollow carbon structure (OLCS, Figs. 2c and S3). The strong magnetic property of Co@carbon disappears in OLCS (Fig. 2d). XRD spectra (Figs. S4–S6) confirm that the post-treatment successfully transforms the zerovalent cobalt into cobalt phosphide and oxides in the carbon spheres. Nitrogen dopants (7.8–11.1 at.%) are simultaneously incorporated into the carbon layers during the graphitization process (Fig. S7 and Table S1). Since Co_3O_4 @carbon was annealed in air to supply oxygen to yield cobalt oxide, the combustion process might result in the undetectable content of nitrogen in the derived hybrids. Compared with the high specific surface area (SSA) of PBA-CoCo ($675.3 \text{ m}^2/\text{g}$, Fig. S8), the SSAs of the hybrid materials are reduced to 27.7 – $47.5 \text{ m}^2/\text{g}$ due to the collapse of porous PBA structure, whereas OLCS yields a high SSA of $564.0 \text{ m}^2/\text{g}$ thanks to the hollow structure.

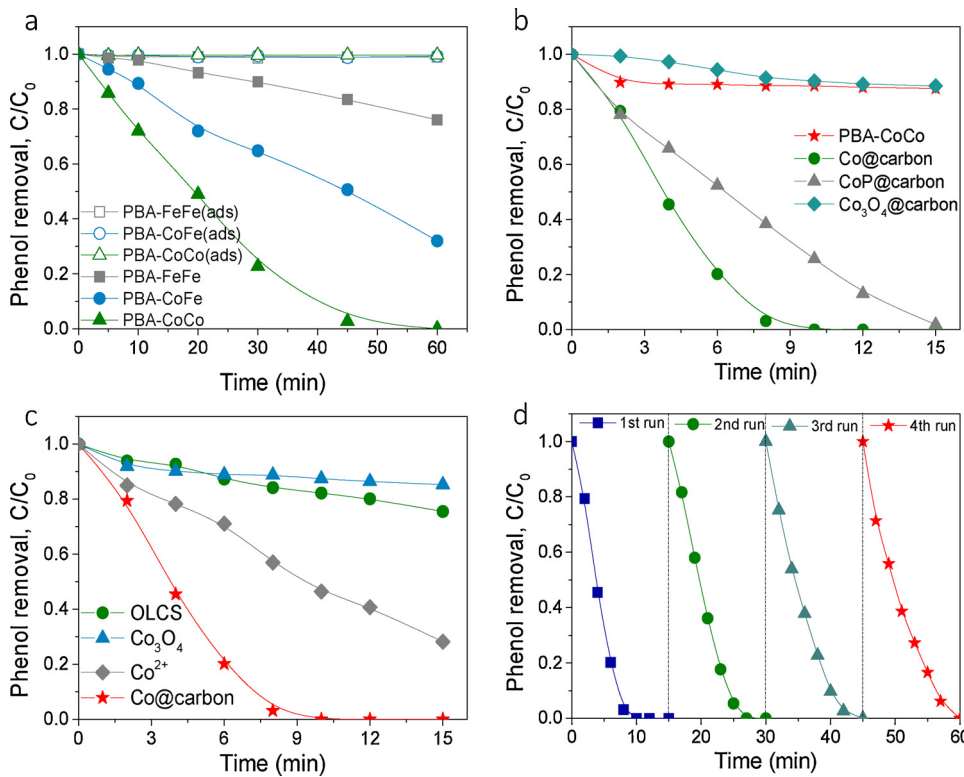
3.2. Evaluation of the catalytic performances

The synthesized carbocatalysts are evaluated for PMS activation to generate reactive ROS for purifying phenol solution. As depicted in Fig. 3a, three PBAs of $\text{Fe}^{\text{II}}/\text{Fe}^{\text{III}}$ (PBA-FeFe), $\text{Co}^{\text{II}}/\text{Fe}^{\text{III}}$ (PBA-CoFe), and $\text{Co}^{\text{II}}/\text{Co}^{\text{III}}$ (PBA-CoCo) are compared, which manifest negligible organic adsorption yet distinguishable catalytic performances. PBA-FeFe and PBA-CoFe attain 24.0% and 68.0% phenol oxidation accordingly, and PBA-CoCo achieves 100% phenol removal in 60 min. No synergistic effect is observed for the dual-metal (Co-Fe) based PBA and cobalt-based PBA is more favorable for PMS activation. This can be attributed to the exclusive catalytic activity of cobalt in PMS-based AOPs, which

surpasses other transition metals/oxides in sulfate-radical-based AOPs (SR-AOPs) in both homogenous ($\text{Co}^{2+}/\text{PMS}$) and heterogeneous ($\text{Co}_3\text{O}_4/\text{PMS}$) reactions [27,28].

Then, PBAs are transformed to carbon hybrids embedded with different zerovalent metals, phosphates and oxides under thermal pyrolysis conditions, and then employed as heterogeneous catalysts in PMS activation. PBA-FeFe and its derivatives presented poor catalytic performances (Fig. S9). In contrast, the reactivity can be considerably enhanced in PBA-CoFe (Fig. S10) and PBA-CoCo (Fig. S11) derived hybrids. Similar to their parent PBAs, the reactivity follows an order of $\text{Fe}@carbon < \text{CoFe}@carbon < \text{Co}@carbon$. Since Co@carbon manifests ultrahigh catalytic performance with complete phenol oxidation in just 5 min, a lower catalyst loading (0.05 g/L) and PMS dosage (0.5 g/L) and a higher phenol concentration (20 ppm) are applied to reduce the reaction rate for comparing the reactivities of different hybrids. As a result, Co@carbon delivers the highest catalytic activity among the composites with 100% phenol degradation in 10 min (Fig. 3b), followed by 98.1%, 12.4% and 11.5% organic removals over CoP@carbon, PBA-CoCo and Co_3O_4 @carbon, respectively. In addition, Fig. 3c shows that Co@carbon is much more reactive than the hollow carbons (OLCS) after removing the encased metal NPs and outperforms the two benchmark SR-AOPs systems of $\text{Co}^{2+}/\text{PMS}$ and $\text{Co}_3\text{O}_4/\text{PMS}$ with 71.8% and 14.8% phenol degradations, respectively. The poor reactivity of OLCS can be attributed to the low graphitic degree derived under a mild pyrolysis temperature (500 °C). Therefore, it is concluded that metal@carbon hybrids deliver much better carbocatalysis than its sole counterparts attributed to the synergistic effects within the composites, and the metal species can tailor the reactivity of carbon spheres during the catalytic oxidation.

The reusability of heterogeneous catalysts in AOPs is of critical significance in practical applications. Previous studies have indicated that the stability of graphene-based materials is typically unsatisfactory [29,30]. This is due to the vulnerable edges and surface functionalities in oxidative environment and coverage of active sites by reaction



intermediates via hydrogen bonds and/or strong $\pi - \pi$ interactions. Fig. 3d indicates that the Co@carbon exhibits outstanding stability, maintaining 100% phenol oxidation in four successive cycles. The exceptional reusability of the composites is supposed to be attributed to several aspects. Firstly, the closed fullerene shells provide a robust carbon framework with a low level of structural defects, which helps resist the ROS oxidation from the boundaries and vacancies to preserve the reductive nature of the carbon lattice. Secondly, the spherical and intact carbon sphere of Co@carbon maximizes the exposure of surface active sites (nitrogen dopants and activated sp^2 carbons) compared with the severely stacked graphene layers, which not only provides facile access of catalytic centers to the reactants (PMS) but also facilitates the desorption and diffusion of the intermediates. Herein, surface accumulation of reaction intermediates and their coverage of reactive sites can be effectively alleviated. Thirdly, the formation of core/shell configuration secures the superb reactivity of TM@carbon in carbocatalytic oxidation. The incorporated cobalt NPs can excite electrons to the adjacent carbon surface, which enriches and compensates the charge population of fullerene surface for continuous PMS activation and resisting against carbon oxidation. The electron-rich and reductive carbon sphere is the key in the redox process during PMS activation, which will be elaborated in the following mechanistic discussions. Fourthly, the carbon shells provide a confinement environment to protect cobalt NPs from corrosion by reacting with oxygen, moisture and acid environment ($pH \approx 3.2$ at $[PMS] = 0.5 \text{ g/L}$) to maintain the metallic property of Co NPs. Recent DFT calculations witnessed that metal-carbon/nitrogen bonds will be formed at the interfaces between metal terminations and carbon surface [21,23]. These chemical bindings may also prevent the cobalt leaching during the reaction. In addition, the magnetic metal core makes the Co@carbon be easily removed from the reaction solution in the presence of an external magnet (Fig. S12).

3.3. Mechanistic investigation

In order to probe the reactive species during PMS activation over the developed carbocatalysts, the competitive radical quenching test is

Fig. 3. (a) Adsorptive and catalytic phenol removals by different PBA catalysts. ($[PMS] = 1.0 \text{ g/L}$, $[\text{catalyst}] = 0.1 \text{ g/L}$, $[\text{phenol}] = 10 \text{ ppm}$) Reactivity comparison of Co@carbon with (b) PBA-CoCo and other hybrids, (c) sole carbon OLCS (after removal of metallic core in Co@carbon) and benchmark $\text{Co}^{2+}/\text{PMS}$ and $\text{Co}_3\text{O}_4/\text{PMS}$ systems, (d) stability. ($[PMS] = 0.5 \text{ g/L}$, $[\text{catalyst}] = 0.05 \text{ g/L}$, $[\text{phenol}] = 20 \text{ ppm}$).

performed by employing different radical scavengers to determine the roles of radicals in phenol oxidation. Methanol (MeOH) with an α -H atom on the carbon center connected to $-\text{OH}$ is capable of rapidly quenching both $\text{SO}_4^{\cdot-}$ ($k_{\text{MeOH-SO}_4^{\cdot-}} = 1.6-7.7 \times 10^7$) and $\cdot\text{OH}$ ($k_{\text{MeOH-OH}} = 1.2-2.8 \times 10^9$) with high rate constants [31]. In contrast, tert-butanol (TBA) without α -H is prone to react with $\cdot\text{OH}$ ($k_{\text{TBA-OH}} = 3.8-7.6 \times 10^8$) rather than $\text{SO}_4^{\cdot-}$ ($k_{\text{TBA-SO}_4^{\cdot-}} = 4.0-9.1 \times 10^5$) [32]. Thus, the contributions of the two radicals in phenol oxidation can be elucidated by comparing the changes of the reaction rates upon the addition of the different radical quenching agents. Fig. 4 presents that the presence of TBA (200 times mole ratio of PMS) merely affects the reaction rate compared to the control group (without MeOH or TBA), and that 100% phenol removal can still be realized in 10 min. However, the scenario for MeOH is different and the addition of MeOH

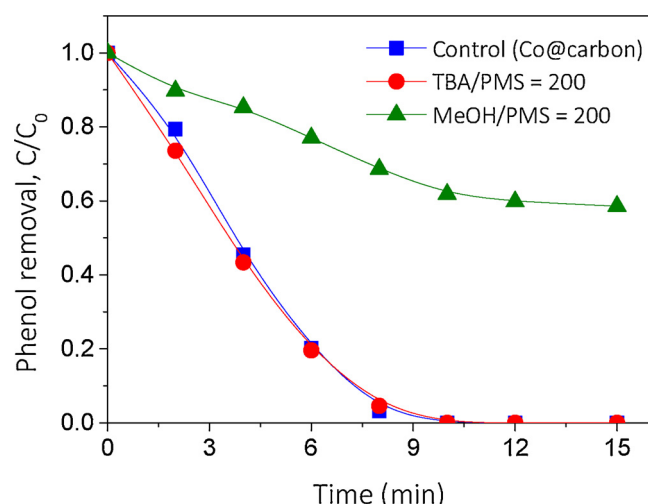


Fig. 4. Radical quenching tests with addition of TBA or MeOH into the Co@carbon/PMS system. ($[PMS] = 0.5 \text{ g/L}$, $[\text{catalyst}] = 0.05 \text{ g/L}$, $[\text{phenol}] = 20 \text{ ppm}$, $[\text{temperature}] = 25^\circ\text{C}$).

Table 1

Summary of the theoretical calculation results of the coupling effects in the hybrids and the catalytic performances for PMS activation.

Configuration	l_{O-O} (Å)	E_{ads} (eV)	$Q(e)$ G to PMS	E_{adh} (eV)	$Q(e)$ slab to G
Free PMS	1.35	–	–	–	–
G	1.41	–1.26	0.55	–	–
Co@G	1.48	–2.45	0.96	–3.96	0.88
CoP@G	1.43	–1.27	0.56	–1.68	–0.03
Co ₃ O ₄ @G	1.39	–0.81	0.44	–1.84	–0.17
NG	1.47	–3.36	0.96	–	–
Co@NG	1.47	–2.36	0.95	–5.10	0.78
CoP@NG	1.44	–1.99	0.70	–2.79	–0.62
Co ₃ O ₄ @NG	1.42	–1.71	0.62	–2.98	–0.76

dramatically slows down the phenol oxidation with only 41% phenol oxidation. The profound influence of MeOH and insignificant impact of TBA indicate that sulfate radicals are the dominant reactive species accounting for the catalytic degradation in Co@carbon/PMS system. A similar mechanism is also discovered in the PBA-CoCo/PMS system (Fig. S13).

To gain further mechanistic insights into the catalytic processes, theoretical computations are performed to mimic PMS adsorption over different graphene and metal@graphene hybrid models. Since a heterogeneous PMS activation process typically involves several steps including PMS adsorption, electron migration from the catalyst to PMS, and cleavage of peroxide O–O bond to generate free radicals. Three key factors of O–O bond length (l_{O-O}), adsorption energy (E_{ads}), and number of electron transfer (Q) are calculated. For the single slabs, N-doping into the graphene (NG) can impressively enhance the PMS adsorption with a greater electron transfer and prolonged O–O bond than G (Table 1 and Fig. S14). N dopants can cause a dipole moment at the local domain, giving rise to positively charged carbon atoms adjacent to the negatively charged nitrogen atom because of their differences in electronegativities (Fig. S15) [33]. The activated carbon atoms are much favorable for binding with the oxygen atoms for promoted PMS activation. Then, graphene clusters (G and NG) are coupled with metal slabs to mimic the metal@carbon hybrids in this work as shown in Figs. 5 and S16, respectively. It is discovered that Co@G significantly enhances the adsorption ($E_{ads} = -2.45$ eV) compared with single G (-1.26 eV), suggesting that the formation of heterostructure can enhance the interactions between carbon and PMS, leading to preferable cleavage of O–O bond (1.48 Å vs 1.41 Å of G) and more charge transfer (0.96 e vs 0.55 e of G) to evolve free radicals. However, bearing CoP and Co₃O₄ slabs beneath the graphene attains limited promotion in l_{O-O} , E_{ads} and Q. Similar scenarios are also observed for the metal@NG models. Generally, the synergistic effects in nanohybrids follow the sequence of Co > CoP > Co₃O₄, which is in good agreement with their catalytic performances in the experiment. Therefore, constructing zerovalent metal under graphitic layers may be the most promising model to realize a high-performance hybrid catalyst for advanced oxidation. Notably, the carbon outer sphere in the hybrids not only mediates the electron transfer from metal to PMS but also activates the persulfate as a catalyst to promote the PMS adsorption and cleavage of peroxide O–O bond. Thus, the TM@carbon-driven AOPs still depend on the manipulated carbocatalysis in nature.

Nevertheless, Co@G and Co@NG present similar catalytic reactivities in PMS activation, and the N-doping can promote the catalytic performances of CoP@NG and Co₃O₄@NG hybrids in comparison to CoP@G and Co₃O₄@G (Table 1). More importantly, Co@NG exhibits weaker adsorption (-2.36 eV) compared with NG (-3.36 eV). In previous studies, it is discovered that N-doping into graphene and carbon nanotubes would induce a nonradical pathway where persulfates will be activated and confined on the carbon surface and oxidize the contaminants directly via an electron-mediation regime through the conductive carbon [34–37]. Distinctly, radical quenching tests imply that

Co@carbon/PMS is a sulfate radical based system. Therefore, the encapsulated metal nanoparticles tailor the carbon surface toward moderate PMS adsorption with great electron migration, which benefits to releasing the cleaved PMS into bulk solution as free radicals and enabling the hybrid-driven oxidation in a radical manner.

Herein, the catalytic activity of the carbon lattice may be determined by the embedded metal species. Both the experimental and theoretical studies indicate that the catalytic activities of the hybrids in PMS activation follow the order of Co > CoP > Co₃O₄, in coupling with both G and NG. It is reasonable to speculate that the metal terminations may regulate the electronic states of the interacted carbon sphere, which subsequently govern the catalytic behavior of carbons in redox reactions. The DFT calculations unveil that Co termination manifests the greatest adhesion energy when its coupling with G (-3.96 eV) compared with CoP (-1.68 eV) and Co₃O₄ (-1.84 eV), suggesting the stronger interactions between the two compounds (G and metal slab). Such a synergistic effect can be further enhanced upon coupling with N-doped carbon cluster (-5.10 eV). Additionally, significant electron migration is experienced from cobalt surface to G (0.88 e) and NG (0.78 e), which can enrich the electron population of the carbon lattice to facilitate charge transportation to PMS. In contrast, CoP and Co₃O₄ cannot contribute electrons. Thus, the electron migration capacity of the metal slabs to carbon layers can lie in several aspects. Firstly, cobalt possesses a much lower work function (4.41 eV, Fig. S17) in contrast with CoP (5.06 eV, Fig. S18) and Co₃O₄ (5.33 eV, Fig. S19). The work function represents the energy barrier to excite an electron to the vacuum level and escape from the solid surface [38]. Therefore, cobalt surface is more favorable to deliver electrons to carbon. Secondly, the electrochemical analysis in Fig. S20 indicates that the conductivity of the three pure metal slabs follows an order of Co > CoP > Co₃O₄, which is also in line with their catalytic activities in the redox reactions (Fig. S21). The good conductivity of the encapsulated metals can facilitate the electron migration from the metal slabs to carbon. Thirdly, strong Co-C bonds are witnessed between Co [111] grain boundary and G/NG clusters (Figs. 5 and S16), whereas no such bonds are formed over CoP and Co₃O₄ terminations. These covalent bonds may serve as high-speed tunnels to facilitate charge migration to carbon via inner-sphere electron transfer, which is more effective than the weak van der Waals interactions between CoP/Co₃O₄ and G/NG. Therefore, the gaps in work function and electron transfer capacities of the metal terminations to carbon may be the keys to regulating the electron configuration of the outer carbon shell in TM@carbon hybrids. N-doping can further tune the electron culture (density, distribution and conductivity) and elevate the density of states at Fermi level of graphene for promoted carbocatalysis [25]. Therefore, the integration of metal encapsulation and heteroatom doping synergistically determine the chemical potentials of the carbon surface in hybrids for effectively catalyzing PMS activation. Similar rules should be applicable to other transition metal-based hybrids (e.g. Fe, Mn, Co). It should be noted that the graphene defects, curvature and thickness can induce local strains, tune the carbon electronic structure as well as govern the charge penetration between carbon and metal slabs, which deserve further investigations especially from the theoretical perspective [14,22,39,40].

4. Conclusions

In summary, magnetic TM@carbon composites can be fabricated from Prussian blue precursors with the embedded metal species and fine-tuned by facile post-treatment. The hybrid materials are employed for activating PMS to evolve highly reactive sulfate radicals for phenol decontamination. The Co@carbon demonstrates the best catalytic reactivity and superb stability in phenol degradation and stands out among the diverse PBAs and hybrid materials, thanks to robust N-doped carbon framework and encapsulated metallic cobalt particles. Both experimental and theoretical investigations indicate that the intrinsic

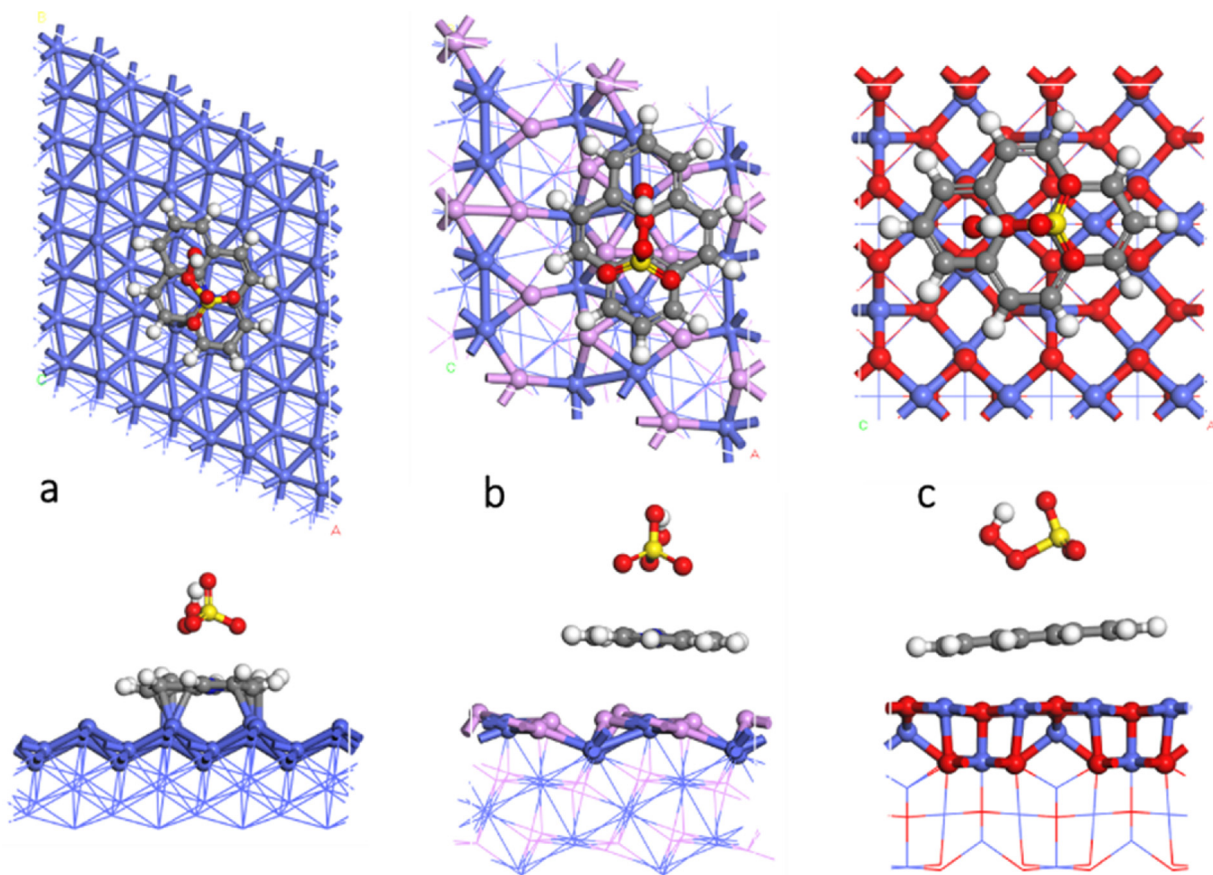


Fig. 5. DFT configurations of PMS adsorption onto Co@NG (a), CoP@NG (b), and Co₃O₄@NG (c).

catalytic activity of the hybrid catalysts in PMS activation is determined by the electronic states of the carbon lattice, which can be rationally regulated by the metal crystals. The study provides novel composite materials for green oxidation and envisages the mechanistic insights into synergistic effects of TM@carbon hybrids in controlling the chemical flexibility of carbocatalysis.

Acknowledgements

The authors appreciate the financial supports from the Australian Research Council (DP190103548) and Open Research Projects from State Key Laboratory (SKL-ChE-16C05 and QAK201808). We also acknowledge the financial supports from the National Science Foundation of China (NSFC, Nos. 21777033, 91645122) and Science and Technology Program of Guangdong Province (2017B020216003).

Appendix A. Supplementary data

Supplementary material related to this article can be found, in the online version, at doi:<https://doi.org/10.1016/j.apcatb.2019.117795>.

References

- [1] B.C. Hodges, E.L. Cates, J.H. Kim, *Nat. Nanotechnol.* 13 (2018) 642–650.
- [2] P. Hu, M. Long, *Appl. Catal. B* 181 (2016) 103–117.
- [3] W.-D. Oh, Z. Dong, T.-T. Lim, *Appl. Catal. B* 194 (2016) 169–201.
- [4] K.B. Zhou, Y.D. Li, *Angew. Chem. Int. Ed.* 51 (2012) 602–613.
- [5] H.Q. Sun, H.M. Ang, M.O. Tade, S.B. Wang, *J. Mater. Chem. A* 1 (2013) 14427–14442.
- [6] S. Navalon, A. Dhakshinamoorthy, M. Alvaro, M. Antonietti, H. Garcia, *Chem. Soc. Rev.* 46 (2017) 4501–4529.
- [7] X.G. Duan, H.Q. Sun, S.B. Wang, *Acc. Chem. Res.* 51 (2018) 678–687.
- [8] C. Nie, Z. Ao, X. Duan, C. Wang, S. Wang, T. An, *Chemosphere* 206 (2018) 432–438.
- [9] P.D. Hu, H.R. Su, Z.Y. Chen, C.Y. Yu, Q.L. Li, B.X. Zhou, P.J.J. Alvarez, M.C. Long, *Environ. Sci. Technol.* 51 (2017) 11288–11296.
- [10] X. Chen, W.-D. Oh, Z.-T. Hu, Y.-M. Sun, R.D. Webster, S.-Z. Li, T.-T. Lim, *Appl. Catal. B* 225 (2018) 243–257.
- [11] S. Navalon, A. Dhakshinamoorthy, M. Alvaro, H. Garcia, *Chem. Rev.* 114 (2014) 6179–6212.
- [12] D.S. Su, G.D. Wen, S.C. Wu, F. Peng, R. Schlogl, *Angew. Chem. Int. Ed.* 56 (2017) 936–946.
- [13] J. Deng, D.H. Deng, X.H. Bao, *Adv. Mater.* 29 (2017) 1606967.
- [14] D.H. Deng, K.S. Novoselov, Q. Fu, N.F. Zheng, Z.Q. Tian, X.H. Bao, *Nat. Nanotechnol.* 11 (2016) 218–230.
- [15] Y.J. Yao, H. Chen, J.C. Qin, G.D. Wu, C. Lian, J. Zhang, S.B. Wang, *Water Res.* 101 (2016) 281–291.
- [16] H.R. Li, J.Y. Tian, Z.G. Zhu, F.Y. Cui, Y.A. Zhu, X.G. Duan, S.B. Wang, *Chem. Eng. J.* 354 (2018) 507–516.
- [17] J. Kang, H.Y. Zhang, X.G. Duan, H.Q. Sun, X.Y. Tan, S.M. Liu, S.B. Wang, *Chem. Eng. J.* 362 (2019) 251–261.
- [18] X.N. Li, Z.M. Ao, J.Y. Liu, H.Q. Sun, A.I. Rykov, J.H. Wang, *ACS Nano* 10 (2016) 11568–11540.
- [19] A. Ajaz, J. Masa, C. Rösler, W. Xia, P. Weide, A.J.R. Botz, R.A. Fischer, W. Schuhmann, M. Muhler, *Angew. Chem. Int. Ed.* 55 (2016) 4087–4091.
- [20] D.H. Deng, L. Yu, X.Q. Chen, G.X. Wang, L. Jin, X.L. Pan, J. Deng, G.Q. Sun, X.H. Bao, *Angew. Chem. Int. Ed.* 52 (2013) 371–375.
- [21] J. Deng, L. Yu, D.H. Deng, X.Q. Chen, F. Yang, X.H. Bao, *J. Mater. Chem. A* 1 (2013) 14868–14873.
- [22] X.G. Duan, Z.M. Ao, H.Y. Zhang, M. Saunders, H.Q. Sun, Z.P. Shao, S.B. Wang, *Appl. Catal. B* 222 (2018) 176–181.
- [23] J. Deng, P.J. Ren, D.H. Deng, L. Yu, F. Yang, X.H. Bao, *Energy Environ. Sci.* 7 (2014) 1919–1923.
- [24] X.K. Kong, C.L. Chen, Q.W. Chen, *Chem. Soc. Rev.* 43 (2014) 2841–2857.
- [25] H.T. Liu, Y.Q. Liu, D.B. Zhu, *J. Mater. Chem.* 21 (2011) 3335–3345.
- [26] D. Aguila, Y. Prado, E.S. Koumousi, C. Mathoniere, R. Clerac, *Chem. Soc. Rev.* 45 (2016) 203–224.
- [27] G.P. Anipsitakis, D.D. Dionysiou, *Environ. Sci. Technol.* 37 (2003) 4790–4797.
- [28] G.P. Anipsitakis, D.D. Dionysiou, *Environ. Sci. Technol.* 38 (2004) 3705–3712.
- [29] D.G. Li, X.G. Duan, H.Q. Sun, J. Kang, H.Y. Zhang, M.O. Tade, S.B. Wang, *Carbon* 115 (2017) 649–658.
- [30] X.G. Duan, H.Q. Sun, Z.M. Ao, L. Zhou, G.X. Wang, S.B. Wang, *Carbon* 107 (2016) 371–378.
- [31] X.G. Duan, C. Su, J. Miao, Y.J. Zhong, Z.P. Shao, S.B. Wang, H.Q. Sun, *Appl. Catal. B* 220 (2018) 626–634.
- [32] C.J. Liang, H.W. Su, *Ind. Eng. Chem. Res.* 48 (2009) 5558–5562.

- [33] X.G. Duan, Z.M. Ao, D.G. Li, H.Q. Sun, L. Zhou, A. Suvorova, M. Saunders, G.X. Wang, S.B. Wang, *Carbon* 103 (2016) 404–411.
- [34] X.G. Duan, H.Q. Sun, Z.P. Shao, S.B. Wang, *Appl. Catal. B* 224 (2018) 973–982.
- [35] S.S. Zhu, X.C. Huang, F. Ma, L. Wang, X.G. Duan, S.B. Wang, *Environ. Sci. Technol.* 52 (2018) 8649–8658.
- [36] J. Yu, L. Tang, Y. Pang, G. Zeng, J. Wang, Y. Deng, Y. Liu, H. Feng, S. Chen, X. Ren, *Chem. Eng. J.* 364 (2019) 146–159.
- [37] L. Tang, Y. Liu, J. Wang, G. Zeng, Y. Deng, H. Dong, H. Feng, J. Wang, B. Peng, *Appl. Catal. B* 231 (2018) 1–10.
- [38] A. Kahn, Fermi level, work function and vacuum level, *Mater. Horiz.* 3 (2016) 7–10.
- [39] J. Zhang, Y. Cheng, S.F. Lu, L.C. Jia, P.K. Shen, S.P. Jiang, *Chem. Commun.* 50 (2014) 13732–13734.
- [40] G.L. Chai, Z.F. Hou, D.J. Shu, T. Ikeda, K. Terakura, *J. Am. Chem. Soc.* 136 (2014) 13629–13640.